Simulating Wind Fields and Snow Redistribution Using Terrain-Based Parameters to Model Snow Accumulation and Melt Over a Semi-Arid Mountain Catchment

ADAM WINSTRAL[1] AND DANNY MARKS[1]

ABSTRACT. In mountainous regions, wind plays a prominent role in determining snow accumulation patterns and turbulent heat exchanges strongly affecting the timing and magnitude of snowmelt runoff. In this study, digital terrain analysis was employed to quantify aspects of the upwind topography related to wind shelter and exposure, to efficiently develop a distributed time-series of snow accumulation rates and wind speeds to force a distributed snow model. Parameters are presented that determined each grid cell's topographic exposure and potential for drift development relative to observed winds. Using meteorological data taken from both an exposed and a sheltered site in the Reynolds Mountain East watershed (0.38 km^2) in southwestern Idaho, the terrain parameters were used to distribute rates of snow accumulation and wind speeds at an hourly time-step for input to ISNOBAL, an energy and mass-balance snow model. Model runs were initiated prior to the development of the seasonal snow cover and continued through complete meltout for the 1986 (precipitation 128% of average), 1987 (66%), and 1989 (108%) water years. A comprehensive dataset consisting of a time-series of aerial photographs taken during meltout, measured runoff, and snow data from the sheltered meteorological site were used to validate the simulations. ISNOBAL forced with accumulation rates and wind fields generated from the applied terrain parameterizations accurately modeled the observed snow distribution including the formation of drifts and scoured wind-exposed ridges, and snowmelt runoff for all three years of study. By contrast, ISNOBAL forced with spatially constant accumulation rates and wind speeds taken from the sheltered meteorological site, a typical snow-monitoring site, overestimated peak snowmelt inputs and tended to underestimate snowmelt inputs prior to the runoff peak.

Keywords: distributed modeling, snow redistribution, digital terrain analysis, runoff

1. INTRODUCTION

In mountainous basins, snow distribution exhibits tremendous spatial heterogeneity (Elder *et al.*, 1991; Doesken and Judson, 1996; Luce *et al.*, 1998; Balk and Elder, 2000). The disparate nature of snow distribution, an effect of both accumulation and melt differences, consequently affects snowmelt runoff patterns. Snow accumulation disparities in alpine basins are largely a function of wind redistribution (Elder *et al.*, 1991; Blöschl and Kirnbauer, 1992; Luce *et al.*, 1998; Prasad *et al.*, 2001; Winstral *et al.*, in press), while snowmelt contributions are additionally affected by spatially varying energy fluxes (Elder *et al.*, 1991; Marks *et al.*, 1998, 2001; Marks and Winstral, 2001). Spatially and temporally varying meltwater production can strongly influence discharge (Seyfried and Wilcox, 1995; Luce *et al.,* 1998), plant communities and ecology (Barron *et al.,* 1993, Flerchinger and Cooley, 2000), water chemistry (Woolford *et al.*, 1996), and hillslope erosion (Tarboton *et al.,* 1991)

Though wind induced snow redistribution has often been cited as one of the strongest influences on snow accumulation patterns, very few studies have directly examined the relative impact of

[1] Northwest Watershed Research Center, United States Department of Agriculture-Agricultural Research Service, 800 Park Blvd., Suite 105, Boise, ID 83712.

redistribution data, or lack thereof, upon hydrologic modeling of mountainous basins. Those that have have indicated the crucial need to account for this process. Luce *et al.* (1998) derived drift factors based on extensive snow surveys to drive the Utah Energy Balance Snow Accumulation and Melt model (Tarboton and Luce, 1996) to examine the influence of snow drifting upon runoff predictions. They found that differences in solar radiation and temperature alone were not great enough to explain the observed heterogeneity of snow distribution and only the model that did account for drifting predicted significant melt coinciding with the observed rise of the hydrograph. In another study, Winstral *et al.* (in press) found that terrain-based parameterizations of wind exposure and shelter explained substantially greater amounts of the observed variance in snow distribution than solar radiation input and elevation.

While recognized as a dominant control on snow accumulation and an integral component of hydrologic modeling of alpine basins, explicit representations of the redistribution process within distributed accumulation and melt models of alpine snow distribution have been limited. Luce *et al.* (1998) were able to account for drifting in their distributed modeling only through the use of extensive survey data, which is costly, time-consuming and spatially limited (Elder *et al.*, 1991; Davis *et al.*, 2001). While physically-based, continuous models of snow redistribution have been developed for flat to gently rolling terrain (e.g. Prairie Blowing Snow Model (Pomeroy *et al.,* 1993); SnowTran-3D (Liston and Sturm, 1998)), extension of these findings to alpine terrain has been limited by the complexity of alpine wind fields and the computational intensity of the models themselves. Prasad *et al.* (2001) sought to establish a relationship between the empirical drift factors derived by Luce *et al.* (1998) and accumulation patterns modeled with SnowTran-3D finding that though the snow distribution patterns had some similarities, pointwise comparisons produced significant errors. In the Prasad *et al.* (2001) application, SnowTran-3D was operated in its least complex state, calculating wind fields from empirical wind-topography relationships (e.g. Ryan*,* 1977) forced with a single wind direction and speed.

Recognizing the link between topography and wind (Ryan, 1977, Berg, 1977; Kind, 1981; Barry, 1992; and others), and the ease of terrain modeling compared to wind field based redistribution models, researchers have sought to parameterize the effects of wind redistribution through terrain analysis. Blöschl *et al.* (1991) addressed wind drift as a function of slope and curvature to interpolate measured SWE values in initializing a snowmelt model, while Purves *et al.* (1998) based a blowing snow model on wind-topography relationships to model snow accumulation patterns. Hartman *et al.* (1999) modeled both accumulation and melt within an application of the Regional Hydro-Ecological Simulation System and used the TOPMODEL-derived topographic similarity index or wetness index to redistribute snow from steep slopes to areas of topographic convergence and low gradients. Cline (1992), Lapen and Martz (1993), and Winstral *et al.* (in press) derived terrain parameterizations specifically aimed at capturing snow redistribution patterns, achieved good results in regression models of snow distribution, and noted the potential benefits of terrain parameterizations as surrogates for the redistribution process.

The terrain parameterizations introduced by Winstral *et al.* (in press) were found to be significant predictors of snow depth accounting for observed snow distribution differences that could not be explained by elevation, solar radiation input, or slope. These parameters were capable of varying the direction of analysis to isolate upwind terrain, could control the upwind extent of terrain analyzed, and were computationally efficient. Winstral (1999) has shown, as Hartman *et al.* (1999) suggested, that terrain parameterizations capable of focusing on upwind conditions are preferred to global parameterizations (e.g. curvature and the TOPMODEL topographic similarity index). The developed parameters were designed to: a) describe the shelter/exposure of each grid cell relative to wind direction and b) delineate areas of potential flow separation. Flow separation zones can occur downwind of ample slope breaks, producing large snowdrifts that can be an important component of alpine water storage (Barry, 1992). Previous modeling efforts have indicated the need for improved means of modeling drift development within flow separation zones (Purves *et al.*, 1998; Prasad *et al.*, 2001).

Marks *et al.* (1998, 2001) and Marks and Winstral (2001) have shown that not only does wind play a vital role in determining accumulation patterns but also in determining turbulent heat fluxes to the snow cover. In rain-on-snow events accompanied by high winds, high melt rates can occur

in wind-exposed regions with very little melt production coming from wind-sheltered areas (Marks *et al.*, 1998, 2001). To our knowledge only the Susong *et al.* (1999) and Marks *et al.* (1999a) applications of the spatially distributed energy balance snowmelt model, ISNOBAL (Marks *et al.,* 1999a), modeled snow cover turbulent heat fluxes as a function of a spatially varying wind field and this was done purely as a function of elevation.

The goal of this study was to account for the significant wind-induced heterogeneities in snow accumulation and melt in an effective and efficient manner within a time-evolving spatial snow model. We applied the terrain-based parameterizations of redistribution effects developed by Winstral *et al.* (in press) to spatially distribute snow accumulation rates and wind speeds at an hourly time-step within the coupled energy and mass-balance snowmelt model, ISNOBAL (Marks *et al.,* 1999a). The previously developed terrain parameters were calibrated and slightly modified for this research initiative. ISNOBAL has been used to simulate the development and melting of the snow cover over basins varying from 1 to 2500 km^2 (Marks *et al.*, 1999a). The current study modeled snow accumulation and melt from the onset of accumulation in mid-fall to complete meltout for three winter seasons in a small headwater catchment of the Reynolds Creek Experimental Watershed, Idaho. Scouring and drifting of snow, as well as wind speeds were modeled as a function of available meteorological data and the aforementioned redistribution functions for the 1986, 1987, and 1989 water years. These study years were chosen based on the availability of aerial photography depicting the temporal advance of snow-free areas during the ablation season. Validation of spatially distributed snow models is complex but perhaps the single most useful type of validation data is such a time series of snow extent (Davis *et al.*, 2001; Tarboton *et al.*, 2000). Additionally, we compared daily-simulated surface water inputs to the basin hydrograph and point-estimations of snow-water-equivalent to snow pillow and snow course data taken from a site within the research area to further assess model performance.

2. STUDY AREA

2.1 Field Site

The Reynolds Mountain East (RME) study area (0.38 $km^{2\dagger}$) is a headwater catchment within the Reynolds Creek Experimental Watershed (RCEW) in southwestern Idaho. The RCEW, operated by the United States Department of Agriculture – Agricultural Research Service (USDA-ARS) (Robins *et al.*, 1965), has functioned as a field laboratory for hydrologic research since 1960 (Marks, 2001; Slaughter *et al.*, 2001). RCEW, encompassing 239 km^2, has a wide range of elevations (1100 – 2400 masl) with a corresponding strong precipitation gradient. Precipitation patterns are strongly seasonal with typically dry summers and wet winters. Annual precipitation at a site located at 1207 masl is 275 mm with 70% falling in the November – May period while at a site at 2170 masl annual precipitation is 1123 mm with 83% falling during the aforementioned snow accumulation season (Hanson, 2001).

The RME catchment (Figure 1) is the principal high elevation research area for the RCEW. Elevations range from 2027 to 2137 masl with an average slope of 8.2°. Approximately 20% of the RME catchment is forested (split between aspen and mixed conifers) with the remainder of the basin consisting of mixed sagebrush. Prevailing winds out of the southwest (resultant mean wintertime direction is 230°) produce a full range of snow accumulation regimes within the RME catchment including a wind-exposed ridgeline that accumulates very little snow throughout the winter and several substantial lee slope drifts that persist through the late spring supporting the aspen and fir communities. Wind-induced snow redistribution occurs primarily during and immediately following storm periods. Avalanching does not play a role in redistributing snow in this catchment.

† The basin area was computed from a grid-based watershed delineation of the recently updated 10 m DEM for RCEW. The area as defined here reflects the 3,762 10 m grid cells used for basin calculations as part of this study and differs slightly from other published values.

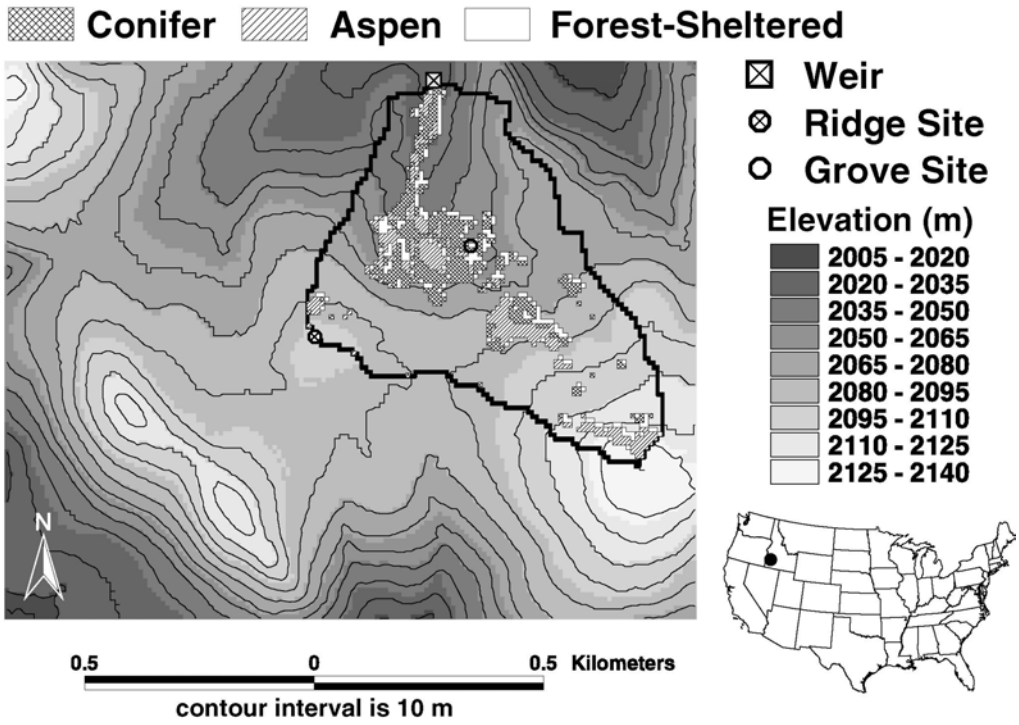

Figure 1. The Reynolds Mountain East (RME) study area and surrounding topography. Only classified conifers and aspens within the basin are shown, while the unclassified regions within RME are mixed sagebrush. The "forest-sheltered" cells are explained further in the Section 3.2.

The RME catchment contains two climate stations: the Reynolds Mountain Climate station (2097 masl) located on a broad shelf at the southwestern edge of the basin and the Reynolds Mountain Snow Pillow site (2061 masl) located within a forest opening typical of most snow-telemetry (SNOTEL) sites in the Western U.S (Figure 1). Heretofore, these two climate stations will be referred to as the "ridge" and "grove" sites respectively. Average wintertime wind speed and snow accumulation at the ridge site is respectively 230% and 55% that measured at the grove site (c.f. Marks and Winstral, 2001). Hourly data on air temperature, humidity, wind, solar radiation, and precipitation from the wind-exposed ridge site along with hourly data on air temperature, wind, precipitation, and soil temperature from the grove site were applied in this study. Precipitation was measured at each site using a dual-gauge system consisting of both unshielded and alter-shielded universal-recording gauges (Hanson, 2001). At the grove site, hourly snow mass measurements were recorded from a snow pillow and manually measured bi-weekly using a Rosen sampler along a standard snow course.

2.2 Study Years

Based on the availability of late season aerial photographs depicting the spatial evolution of meltout, three water years were selected for this study: 1986, 1987, and 1989. Precipitation at the grove site for the 1October – 30June period for the 1986, 1987, and 1989 water years was 1178 mm (128% of average), 606 mm (66%), and 994 mm (108%), respectively. Measured outflow from the catchment for the 1October – 30June period for the 1986, 1987, and 1989 water years was respectively 829 mm/m^2 (152% of average), 221 mm/m^2 (40%), and 698 mm/m^2 (128%).

3. MODELING METHODS

ISNOBAL, further described below, is a grid-based distributed energy balance snowmelt model that simulates snow cover development and ablation from images of distributed meteorological forcing variables. ISNOBAL model runs were initiated on 1October prior to development of the seasonal snowpack and run through the meltout period for the 1986, 1987, and 1989 water years. Grids of the forcing variables were derived from the available meteorological data collected at the ridge and grove sites, a digital elevation model, and a vegetation coverage of the study area. Descriptions of how the measured point data were distributed over the catchment are provided in the subsequent subsections. Included in the wind and precipitation subsections are detailed descriptions of the terrain parameterizations used to characterize wind exposure and shelter that were the basis for distributing the respective observations. The wind forcings are integral to the calculation of the turbulent heat fluxes, while the precipitation forcings in this application include the effects of wind-induced snow redistribution. Some parameters within the exposure/shelter parameterizations were calibrated using the aerial photos. Parameters requiring calibration are identified in the following subsections with the results of the calibration process presented in Section 4.1. As much as possible, calibration was constrained to the 1986 data. The ISNOBAL-simulated distribution of snow-water-equivalence (SWE) was compared to snow cover extent in each aerial photograph to gauge the spatial accuracy of the presented techniques. Simulated surface water inputs were compared to the basin hydrograph to further assess model performance at a finer timescale. The snow pillow and bi-weekly measured snow course at the grove site provided SWE data serving as a point check on modeled SWE.

3.1 ISNOBAL

ISNOBAL (Marks *et al.*, 1999), a two layer coupled energy and mass-balance model designed for applications over DEM grids, was run at an hourly time-step in this study. Based on the work of Anderson (1976), ISNOBAL uses site topographic and vegetation structure, with climate and precipitation data to solve the energy balance, calculate the mass balance, and track the energy state of the snow cover at each grid cell. The forcing variables for the model are: net solar radiation, incoming thermal radiation, air temperature, vapor pressure, soil temperature, wind speed, and precipitation. In this study, wind-induced snow redistribution is accounted for in the precipitation forcings. Modeled outputs of interest to this study were snow mass, snowmelt, and predicted runoff from the base of the snow cover. Predicted runoff includes snowmelt and rain passing through the snow cover, and rain falling on bare ground. To clearly distinguish modeled runoff (the amount of water arriving at the soil surface), from stream discharge (a measure of instream flow), the ISNOBAL-modeled runoff is referred to as surface water input (SWI) in this paper. The subsequent paper (Marks *et al.*, this issue) details the spatial and temporal variance of the energy balance terms and provides a further discussion of the ISNOBAL model. Comprehensive descriptions and details of ISNOBAL can be found in Marks *et al.* (1999a and b).

3.2 Spatial Data

A 10m grid cell digital elevation model derived and processed from USGS contours served as the foundation for the spatial modeling. A 10 m gridded vegetation coverage classified from infrared aerial photography was used to account for canopy effects upon radiation and as a supplement to the topography-based shelter/exposure indices. The vegetation coverage was enhanced to describe canopy-dependent wind sheltered cells immediately downwind of forest cover and within forest openings (see Figure 1). If a mixed sagebrush cell had at least two adjacent upwind cells classified as fir or aspen it was considered to be wind-sheltered. Based on seasonal prevailing winds out of the southwest, the set of upwind cells consisted of adjacent cells to the south, southwest, and west. If at least five of the surrounding cells around a mixed sagebrush cell were either fir, aspen, or fit the just described wind-sheltered definition, it was considered to be a within-forest-opening site and similarly classified as wind-sheltered.

The late-season series of aerial photographs used to determine snow cover extent and evaluate model output were independently processed previous to the current study. Unfortunately, the

photographs no longer exist and all that remains are the classified basin images. Classifications of snow-covered and bare ground areas were based on threshold brightness levels that varied for each scene. While this process appeared to do an excellent job of discerning snow-covered-area in the mixed sagebrush regions, it appeared that some errors were incurred beneath the forest canopy. Geo-registration of snow-covered scenes can be problematic as many typical ground control points (e.g. road intersections) are obscured. The lack of quality ground control points did lead to apparent errors in some of the scenes, however these errors were slight and did not affect evaluation of the model results. In addition, the mask of the RME catchment previously applied to the classified images was different from the current watershed delineation leading to unclassified areas occurring within the catchment.

3.3 Distributed Forcing Fields

3.3.1 Solar Radiation

Theoretical clear sky solar radiation corrected for topography was calculated using the STOPORAD model, the snow cover version of the TOPORAD model (Dozier, 1980; Dozier and Frew, 1981; Dubayah, 1994). STOPORAD uses exoatmospheric solar radiation, a two-stream atmospheric radiative transfer model and a DEM to produce radiation and albedo images for the visible (0.28 – 0.7 μm) and near infrared (0.7 – 2.8 μm) bands. Albedo is calculated for a clean snow cover as a function of sun angle and grain size using empirical relationships described by Warren and Wiscombe (1980), Wiscombe and Warren (1980), and Marshall and Warren (1987) and refined for general application by Marks (1988) and Marks and Dozier (1992). Clear sky images were subsequently corrected for cloud cover, canopy effects, and late-season albedo decay to produce hourly images of solar radiation flux over the snow cover in the following manner. A cloud cover factor, determined from the ratio of measured solar radiation to its theoretical clear sky value at the ridge site was used to split above-canopy radiation into direct and diffuse components. The transfer of direct and diffuse radiation through the canopy was calculated using methods described by Link and Marks (1999). STOPORAD-produced albedos were adjusted downward during the meltout period using a linear decay function to account for the increasing exposure of organic debris beneath the forest canopy (Link and Marks, 1999).

3.3.2 Thermal Radiation

Atmospheric thermal radiation was calculated from air temperature, relative humidity, and elevation and corrected for topographic effects based on a model by Marks and Dozier (1979). The atmospheric contribution to snow cover thermal radiation flux was further adjusted for canopy effects based on the work of Link and Marks (1999). Transmissivity factors (i.e. below canopy sky-view factors) of 0.44 and 0.30 were assigned to the aspen and fir trees respectively. Thermal radiation in the "canopy-dependent wind sheltered" class was slightly enhanced compared to open canopy conditions and were assigned a transmissivity factor of 0.75 to account for edge effects. Canopy emittance was calculated under the assumption that canopy temperature was equal to below-canopy air temperature.

3.3.3 Air Temperature, Vapor Pressure, Soil Temperature

Air temperature data were measured at both the ridge and grove sites, relative humidity (used to calculate vapor pressure) data were available from the ridge site, and soil temperature data were available from the grove site. Air temperatures were lapsed for elevations between that of the two measurement sites with higher and lower elevations receiving the hourly temperatures recorded at the ridge and grove sites, respectively. Measured relative humidity, assumed constant over the catchment, was converted to distributed vapor pressures using the distributed air temperatures based on methods described by Byers (1974). Soil temperatures were assumed to be spatially constant.

3.3.4 Wind

Wind data from the exposed ridge and sheltered grove sites were deemed as representative of the catchment extremes. A series of wind factor images focused on all possible wind directions at 5° increments were established to conduct weighted interpolations of the hourly measured wind data. The basic premise for the wind factor images was that if a cell's exposure, relative to the recorded wind direction, was equal to or greater than the exposure of the ridge meteorological site, it would receive the wind speed as measured at the ridge site. If a cell had equal or greater shelter than that of the grove site it would receive the wind speed registered at the grove site. All other cells received a linearly interpolated value based on the degree of shelter provided by the upwind topography and standing vegetation.

The maximum upwind slope parameter (*Sx*) is a measure of topographic shelter or exposure relative to a particular wind direction (Winstral *et al.*, in press). The *Sx* parameter served as the foundation for developing the wind factor fields with subsequent modifications based on the delineation of flow separation zones and vegetation structure. The *Sx* algorithm examines all cells along a fixed line segment determining the cell that has the greatest upward slope relative to the cell of interest and returns the slope (degrees) between this shelter-defining cell and the cell of interest:

$$Sx_{A,\,dmax}(\mathrm{x}_i,\mathrm{y}_i) = \max\left[\tan^{-1}\left(\frac{\mathrm{ELEV}(\mathrm{x}_v,\mathrm{y}_v)-\mathrm{ELEV}(\mathrm{x}_i,\mathrm{y}_i)}{\left((\mathrm{x}_v-\mathrm{x}_i)^2+(\mathrm{y}_v-\mathrm{y}_i)^2\right)^{0.5}}\right)\right], \tag{1}$$

where A is the azimuth of the search direction, *dmax* determines the lateral extent of the search, $(\mathrm{x_i},\mathrm{y_i})$ are the coordinates of the cell of interest, and $(\mathrm{x_v},\mathrm{y_v})$ are the set of all cell coordinates located along the line segment defined by $(\mathrm{x}_i,\mathrm{y}_i)$, A, and *dmax*. Negative *Sx* values indicate exposure relative to the shelter-defining pixel (i.e. the cell of interest is higher than the shelter-defining pixel). Varying *dmax* altered the extent of terrain analyzed and had a substantial effect on the distribution of *Sx* values that is discussed further in the calibration section. By averaging *Sx* across an upwind window of directions a parameter is fashioned that is more robust to both natural and systematic (e.g. terrain deflection) deviations from the recorded resultant mean data. The mean maximum upwind slope parameter ($\overline{Sx}$) is defined as:

$$\overline{Sx}_{\overline{A},\,dmax}(\mathrm{x}_i,\mathrm{y}_i)\Big|_{A_1}^{A_2} = \frac{1}{n_v}\sum_{A=A_1}^{A_2} Sx_{A,\,dmax}(\mathrm{x}_i,\mathrm{y}_i), \tag{2}$$

where A_1 and A_2 define the outer limits of the upwind window, $\overline{A}$ bisects A_1 and A_2, and n_v is the number of search vectors in the window defined by A_1 and A_2. A 30° upwind window was used for all $\overline{Sx}$ derivations with *Sx* calculated in 5° increments within the window.

The selection of a maximum shelter-producing pixel based on slope is analogous to the determination of solar shading within the horizon function used in radiation modeling (Dozier *et al.*, 1981). Similar applications of the horizon function to estimate wind speeds have been made by Ryan (1977) and Wörlen *et al.* (1999). Ryan's horizon-based wind correction factor, applied by Wörlen *et al.*, employed a limitless search distance (i.e. *dmax* limited only by the constraints of the topographic map) and established a strongly non-linear relationship between measured horizons and wind speeds. Winstral *et al.* (in press) have shown that, as regards snow redistribution, a distance-limited quantification of upwind terrain was preferred, while unpublished work by the current authors has indicated a stronger linear bias in the $\overline{Sx}$ – snow distribution relationship.

The *Sb* parameter measures upwind slope breaks and has been used to delineate potential flow separation zones (Winstral *et al.*, in press). *Sb* takes the difference between relative slope measures of the local and outlying topography to produce a measure of the break in upwind slope. *Sb* is determined using two applications of the *Sx* algorithm to determine a local *Sx* ($Sx_{\,l}$), and an outlying *Sx* ($Sx_{\,o}$). A user-defined separation distance (*sepdist*) determines the cutoff between the two regional *Sx* calculations. *Sx* is determined along an upwind line segment with a maximum search distance (*dmax*) equal to the separation distance (*sepdist*) to determine Sx_l defined as

$$Sx_{1_A}(x_i, y_i) = Sx_{A,sepdist}(x_i, y_i)\,. \tag{3}$$

Sx_o, in this application was defined as the $Sx_{A,1000m}$ of the cell located the separation distance upwind of the cell of interest along each respective search vector and was defined by

$$Sx_{o_A}(x_i, y_i) = Sx_{A,1000m}(x_o, y_o)\,, \tag{4}$$

where $[(x_o - x_i)^2 + (y_o - y_i)^2]^{0.5} \cong sepdist$ and $(x_o,y_o) \in (x_v,y_v)$. The difference between Sx_1 and Sx_o along each search vector determined *Sb*. The average of each vector calculation of *Sb* within the upwind window formed a mean measure of upwind slope break, $\overline{Sb}$, defined by

$$\overline{Sb}_{sepdist}(x_i, y_i)\Big|_{A_1}^{A_2} = \frac{1}{n_v}\sum_{A=A_1}^{A_2}\left[Sx_{1_A}(x_i, y_i) - Sx_{o_A}(x_i, y_i)\right]. \tag{5}$$

A sufficient enough slope break will produce flow separation and a downwind lee eddy zone with relatively lower wind speeds. Using the 1986 aerial photos, *sepdist* and a threshold value of $\overline{Sb}$ were determined that afforded the best possible match of remnant late-season snow accumulations and modeled separation zones.

The first step in creating the wind factor images was to determine minimum and maximum values of $\overline{Sx}$ representative of effective conditions at the ridge and grove sites, resepectively. These selected threshold $\overline{Sx}$ values determined which cells, based on terrain exposure alone, would receive wind speed values equal to those measured at the two respective sites. Determination of effective shelter at the ridge site, unaffected by prominent vegetation, was based solely on its $\overline{Sx}$ value. Effective shelter at the grove site however, is a function of both topography and vegetation. Quantifying the vegetation effects in terms of an effective $\overline{Sx}$ value was therefore guided by image analysis in conjunction with the 1986 data.

$\overline{Sx}$ and $\overline{Sb}$ images were derived for all possible wind directions in 5° increments. Based upon a series of rules, corresponding wind factor images were subsequently created based on the aforementioned images and the vegetation coverage (wind factor images are further addressed in the calibration section with an example provided in Figure 4):

- All $\overline{Sx}$ values less than the minimum and greater than the maximum thresholds were assigned the respective threshold values.
- To improve readability of the wind factor images, the $\overline{Sx}$ images were inversely rescaled to a 1.0 – 2.3 range, so that 1.0 was assigned to cells with maximum shelter and 2.3, the average multiple by which wintertime winds at the ridge site exceed those at the grove site, was assigned to cells with minimum shelter.
- Cells classified as fir-bearing, canopy-sheltered, or whose $\overline{Sb}$ value exceeded the established threshold for flow separation were assigned wind factor values of 1.0.
- Cells classified as aspen-bearing had their wind factors arbitrarily reduced by 30% with the stipulation that no values drop below 1.0.

Wind speeds were distributed at an hourly time-step for input to ISNOBAL. At each time-step, wind speeds, as measured at the grove and ridge sites, were interpolated over the wind factor field centered on the wind direction registered at the ridge site.

3.3.5 Precipitation

The precipitation forcings in this application of ISNOBAL consisted of what is referred to as snow accumulation rates — the sum total of snowfall, scour, and redeposition. Previously, Marks and Winstral (2001) modeled snow accumulation and melt at the grove and ridge meteorological sites using SNOBAL, the point version of ISNOBAL. It was found that alter-shielded precipitation catch at the grove site, shielded from all but extreme redistribution events, under-estimated snowfall totals and a correction for undercatch was necessary. Based on an extensive network of dual unshielded and Alter-shielded precipitation gauges at RCEW (Hanson, 2001) a formula for correcting for undercatch was established (Hanson et al., 1999) and applied to the recorded grove site precipitation. The sum of grove site corrected precipitation for the 1986, 1987, and 1989 study seasons were respectively 122%, 120%, and 119% of the Alter-shielded catch. By comparison, use of the World Meteorological Organization's undercatch correction formula designed for global

applications at a daily time-step (WMO, 1998) applied to the hourly data produced corrections of 125%, 114%, and 118%, respectively. At the exposed ridge site, it was found that the Alter-shielded catch provided the best estimate of actual snow accumulation beside the gauge.

Snow accumulation rates were distributed in a similar fashion to wind speeds; as a function of the terrain-based redistribution parameters, canopy cover, and measured precipitation. Analogous to the function of the wind factor images, accumulation factor images were created for distributing snow accumulation. The ridge site was assumed to be representative of conditions at sites with minimum shelter. The grove site was assumed to be representative of sites with maximum shelter and minimal redeposition.

Additionally, the effects of redeposition had to be accounted for in the accumulation factors and this was done using a drift delineator algorithm that combined the $\overline{Sb}$-defined flow separation zones with a *Sx*-based description of the slope break's upwind exposure. Theoretically, bound by an upper limit, the greater the upwind exposure of the slope break, the greater the snow transport flux at the slope break (Pomeroy *et al.*, 1993), and the greater the downwind redeposition rate. In this application, two types of drifts were modeled based on the upwind exposure of the slope break — large and moderate — with accumulation factors assigned accordingly. The upwind exposure of each slope break was determined in the following manner. First, a *focalmean* function was applied to each directional $\overline{Sx}_{1000\ \mathrm{m}}$ image to determine $\overline{Sx}^{*}$ with each cell of the $\overline{Sx}^{*}$ image consisting of the mean of all $\overline{Sx}_{1000\ \mathrm{m}}$ values within a 50 m radius. Averaging the $\overline{Sx}$ images provided an expansive description of the terrain, smoothing minor features in order to determine a broad-based index of topographic exposure. For each cell located in a modeled flow separation zone, the minimum $\overline{Sx}^{*}$ value (maximum exposure) along an upwind line segment of 200 m plus the separation distance (*sepdist*) applied in the *Sb* calculations was determined. The search was begun at the cell of interest because the actual break in slope can occur anywhere within the "local" region defined by *sepdist*. The additional 200 m further searched the upwind terrain for large-scale features capable of affecting the amount of transported snow reaching the slope break. If min($\overline{Sx}^{*}$) was below a value calibrated from the 1986 images, a large drift was modeled and if min($\overline{Sx}^{*}$) was greater than the calibrated cutoff, a moderate drift was modeled.

The steps in assembling the accumulation factor images followed the procedures for development of the wind factor images with slight modifications (accumulation factor images are further addressed in the calibration section with an example provided in Figure 4):

- All $\overline{Sx}$ values less than the minimum and greater than the maximum thresholds were assigned the respective threshold values.
- To improve readability of the accumulation factor images, the $\overline{Sx}$ images were rescaled to a 0.55 – 1.0 range such that 0.55, the wintertime ratio of ridge/grove precipitation catch was assigned to cells with minimum shelter and 1.0 was assigned to cells with maximum shelter.
- Cells classified as fir-bearing or as canopy-sheltered were assigned accumulation factors of 1.0.
- Cells classified as aspen-bearing had their accumulation factors increased by 43% (the inverse of the 30% decrease applied for the wind factors) with the stipulation that no values exceed 1.0.
- Accumulation factors for the modeled flow separation zones were guided by the distribution of empirical drift factors developed for the Upper Sheep Creek catchment, a slightly drier RCEW sub-basin (Luce *et al.*, 1999; Prasad *et al.*, 2001). If a cell was in a $\overline{Sb}$-defined flow separation zone and its min($\overline{Sx}^{*}$) indicated sufficient exposure at the slope break an accumulation factor of 3.5 was assigned. If a cell was in a $\overline{Sb}$-defined flow separation zone and its min($\overline{Sx}^{*}$) indicated that the slope break itself had some degree of shelter, an accumulation factor of 1.5 was assigned.

While accumulation rates were distributed at an hourly time-step using observed data, storm characteristics were accumulated during each storm period to aid in the distribution process. Inconsistencies in hourly precipitation data at the two sites, possibly attributable to factors such as snow bridging over the orifice causing a delay in delivery of snow mass to the gauge load cell,

were observed. Hence, it was felt that the use of storm-averaged winds in conjunction with hourly measured precipitation provided a better account of storm accumulation rates as compared to distributions based on hourly winds combined with hourly precipitation rates. For each storm period the resultant mean wind direction was calculated and the accumulation factor image associated with said direction was used to distribute measured hourly precipitation during the event. Additionally, ridge and grove site precipitation were accumulated over each storm period to form a ridge/grove precipitation ratio to gauge the degree of redistribution during the storm period.

For each hour of precipitation occurrence, three values were interpolated over the accumulation factor image focused on the prevailing wind direction for the storm period: precipitation at the ridge site for assignment to cells with accumulation factors of 0.55, precipitation at the grove site for assignment to cells with accumulation factors of 1.0, and a multiple of 1.0 – 3.5 of grove site precipitation to cells with the maximum accumulation factor of 3.5. If the ridge/grove precipitation ratio was equal to or less than the long-term average of 0.55, maximum redistribution was assumed and a 3.5 multiple of grove site precipitation was assigned. If the ratio was 0.55 – 1.0, the drift multiplier was linearly adjusted down from 3.5 to a minimum of 1.0. If the ratio was greater than 1.0, the precipitation at the ridge site was assigned. For all rain events, the multiplier was set to 1.0.

Accumulation factor images, as well as the wind factor images, were recalculated throughout the modeling period to include the effects of the accumulating snowpack. Whenever an additional meter of snow depth was accumulated in the deepest of drifts, the accumulated snow depths were added to the DEM and the accumulation and wind factor images recalculated from the snowpack-adjusted DEM. It was hoped that this procedure would allow the drifts to develop in a realistic manner. Theoretically, the upwind portions of the drift would fill first, leading to reductions in $\overline{Sb}$ at the forefront of the drift while creating additional downwind shelter consequently increasing downwind $\overline{Sb}$ values. Applied in this manner, the drifts would gradually extend downwind until the slope break threshold was potentially no longer met and the drift reached an equilibrium state (Tabler, 1994).

4. RESULTS AND DISCUSSION

4.1 Calibration of $\overline{Sx}$ and $\overline{Sb}$

Varying *dmax* had a substantial effect on the distribution of $\overline{Sx}$ values on the exposed west-facing ridge along the northeastern boundary of the catchment. Based on a prevailing wind direction of 230° (the resultant mean wintertime wind direction), increasing *dmax* increased the likelihood of cells located on the west side of the valley being included in $\overline{Sx}$ calculations for pixels located on this exposed slope. Increasing the upwind extent of terrain analyzed effectively increased $\overline{Sx}$ values on the mid and lower slopes of the exposed ridge relative to the upper slope (Figure 2). With *dmax* = 100 m, almost the entire west-facing slope, from ridgetop to stream bottom, was assigned a $\overline{Sx}$ lower than that of the ridge site (Figure 2a) whereas at *dmax* = 1000 m only the ridgeline received a $\overline{Sx}$ value lower than that of the ridge site (Figure 2d). Cells lacking topographic shelter along the southern boundary of the RME catchment were relatively unaffected by changes in *dmax*. Based on a composite of the 12April89, 15April87, and 12May86 photos (see Figures 5, 7, 8) representing the progression of exposed bare ground during the initial meltout phase, *dmax* was set equal to 200 m. While higher values of *dmax* might possibly do a better job of segregating meltout along the west-facing ridge, it would also delay meltout on this ridge relative to the exposed cells along the southern RME boundary, inconsistent with the aerial data. Winstral *et al.* (in press), based on snow survey data from Green Lakes Valley (GLV), CO, similarly found that the relationship between $\overline{Sx}$ and observed snow depths weakened as *dmax* was increased from 100 m to 300 m and beyond.

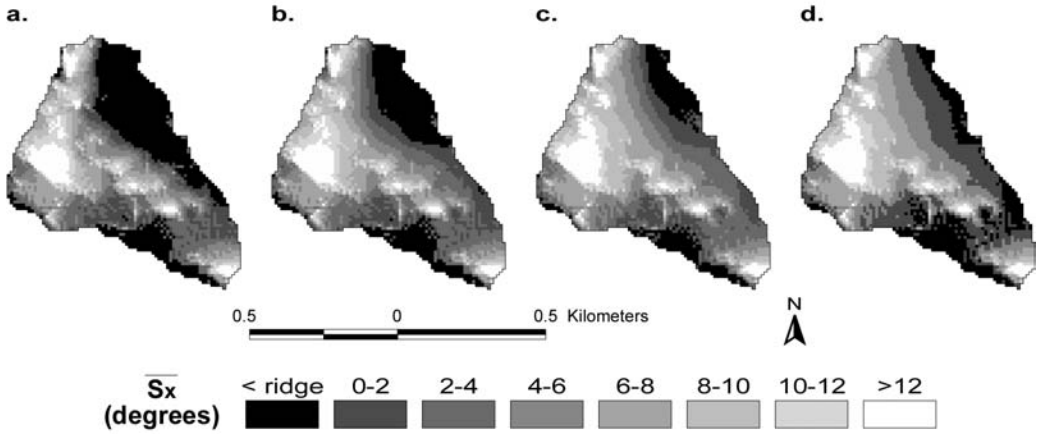

Figure 2. $\overline{Sx}$ calculated from the DEM for the resultant mean wintertime direction of 230° with *dmax* = 100 m (a), 200 m (b), 300 m (c), and 1000 m (d). The "< ridge" classification indicates that a cell is less sheltered/more exposed than the ridge site. As *dmax* increased, $\overline{Sx}$ for cells located along the lower section of the west-facing ridge in the northeast increased relative to the rest of the basin.

The calibration of *sepdist* within the $\overline{Sb}$ calculations and thresold values of $\overline{Sb}$ and $\overline{Sx}^*$ for the delineation of drift zones was based on comparisons of 1986 ISNOBAL modeled results with the associated late season aerial photographs. It was found that *sepdist* = 60 m and a threshold value of $\overline{Sb} > 5°$ was best for determining drift zones, and that a threshold value of $\overline{Sx}^* < 5°$ worked well for differentiating between large and moderate drifts respectively.

Winstral (1999) previously showed that increasing *sepdist* effectively increased the width of the modeled drift zones and that *sepdist* = 300 m and a threshold value of $\overline{Sb} > 7°$ afforded the best relationship between $\overline{Sb}$ -defined drift zones and late season snow distribution in the considerably steeper GLV ($\overline{\text{SLOPE}}$ = 27.6°) (Winstral *et al.*, in press). The authors inferred that the significance of the 300 m *sepdist* might have been affected by avalanching and sloughing of snow coincident with the prevailing wind direction. Furthermore, this previous application of $\overline{Sb}$ was a static snapshot of terrain configuration aimed at characterizing the sum total of seasonal accumulation. By contrast, in the current application "terrain" structure is continuously updated to account for accumulating snow thereby producing modeled drift zones that migrate downwind in time. The 5° $\overline{Sb}$ threshold for determining drift zones applied in the current study delineated 8.2% of the RME catchment as being in a drift zone as calculated directly from the DEM with a prevailing wind direction of 230°. Similar testing of the 7° threshold on the RME DEM classified 5.6% of the catchment as being in a drift zone (Figure 3). The lower threshold increased both the lateral extent of the modeled drift zones and extended the time period over which cells continued to be classified as drifts. The apparent increase in effectiveness of the 5° threshold in this study compared to the 7° threshold previously applied was quite likely the result of the more detailed analysis of low slope gradients provided by this dataset. Revisiting the GLV data found that decreasing the 7° threshold to 5° resulted in only a 10% increase in the number of pixels classified in a drift zone compared to the 46% increase observed in RME. (Note: The Green Lakes Valley study also employed a 10 m grid cell DEM.)

The $\overline{Sx}^*$ parameter was developed to differentiate slope breaks with extended upwind fetch (i.e. large drift zones) from those with only a limited upwind fetch (i.e. moderate drift zones). The necessity of this parameter was made evident in the initial 1986 model runs. It was apparent from the aerial photographs that a small drift area develops in the northwest corner of the catchment coincident with the modeling of a sufficient upwind slope break (see Figures 3 and 5a). The aerial photographs indicated that this drift disappears prior to other drifts in the catchment and the model runs indicated that energy flux differentials were unable to account for the earlier meltout. Terrain analysis indicated that the persistent drifts were just downwind of areas of high exposure whereas the slope break that led to the development of the moderate northwest drift was not nearly as

exposed. The $\overline{Sx}^*$ parameter provided a means of quantifying the exposure of the slope break and the 5° $\overline{Sx}^*$ threshold for differentiating between large and moderate drifts produced model results consistent with observations both within the study area and over the greater southern extent of the Reynolds Creek Experimental Watershed.

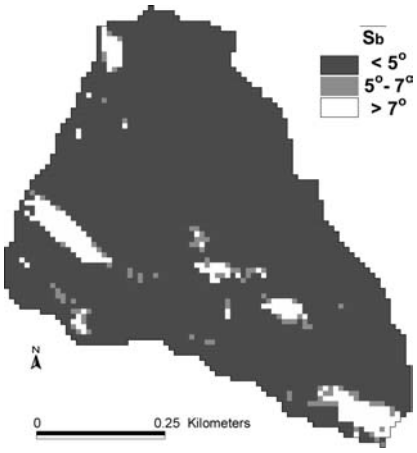

Figure 3. $\overline{Sb}$ calculated from the DEM for the resultant mean wintertime wind direction of 230°. Decreasing the $\overline{Sb}$ threshold for determining drift zones from 7° to 5° resulted in a 46% increase in delineated drift cells.

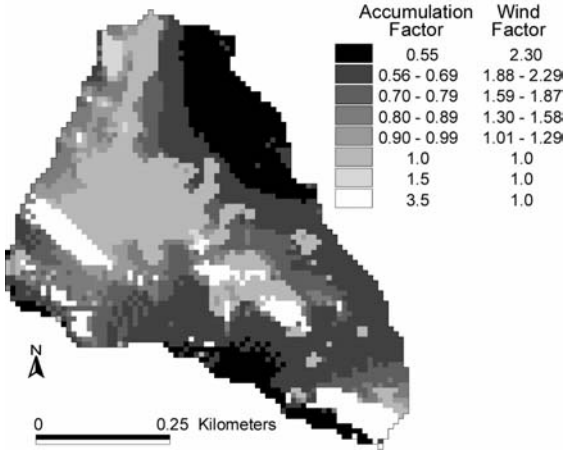

Figure 4. Snow accumulation and wind factors calculated for 230° winds with no snow on the ground. Accumulation and wind factors were derived for all possible wind directions with observations interpolated over the appropriate image.

Examples of wind factor and accumulation factor images calculated with the aforementioned calibrations for 230° winds are shown in Figure 4. Clearly, the exposed ridgelines have the lowest accumulation factors and highest wind factors. The combined effects of vegetative canopy (Figure 1), topographic shelter (Figure 2), and $\overline{Sb}$-defined drift zones (Figure 3) can be seen in the high accumulation – low wind factor regions.

4.2 1986 Water Year

The spatial simulations of snow accumulation and melt for the 1986 water year — October – June precipitation 128% of average; stream discharge 146% of average — closely matched the temporal pattern of advancing bare ground depicted in the aerial photographs (Figure 5a). The timing of the annually consistent pattern of emerging bare ground — complete melting of the snowpack occurring along the west-facing slopes first, advancing through progressively lower energy zones until the only remaining snow is located in drifts — was well represented. Areas classified as bare ground in the 12May86 aerial image that lie within the generally snow covered region in the central basin may well be the product of the influence of the vegetative canopy on captured surface brightness (see Figure 1).

There are four distinct drift areas: the northwest drift located just southwest of the weir, the west drift located southwest of the grove site, the east drift located southeast of the grove site, and the southeast drift (see Figure 5a). It can be inferred from the classified photographs that the northwest drift accumulates the shallowest snow cover amongst the drifts. Though some slight spatial errors can be seen in the location of the modeled drifts — the modeled west drift is slightlyoffset to the west of its actual location, the modeled east drift appears to be slightly small, and the modeled southeast drift may be a little too wide — in general the modeled drifts closely matched their spatial and temporal dispositions. The modeled west drift best exemplifies the end product of the downwind advancing drift zone produced through the inclusion of accumulating snow into the parameter updating process. Similar to naturally occurring drifts, the highest snow-water-

equivalence (SWE) totals can be found at the center of the drift with progressively lower accumulations outwards to the perimeter.

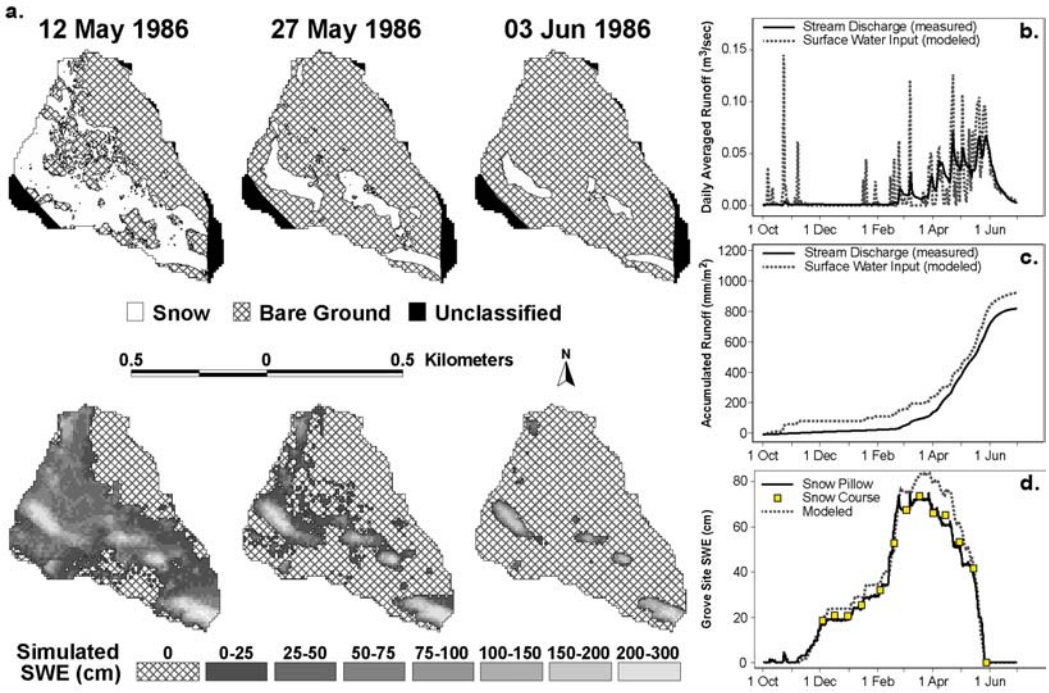

Figure 5. Comparisons of model results and validation data for the 1986 water year. (a) displays the aerial sequence of meltout captured by the aerial photographs across the top and simulated snow-water-equivalent (SWE) across the bottom, (b) compares modeled surface water inputs in units of discharge to outflow at the weir, (c) compares accumulated runoff volumes, and (d) compares modeled to measured SWE at the grove site.

ISNOBAL models melt production in a vertical column at each grid cell. In Figure 5b, the modeled surface water input (SWI) consists of the daily sum of meltwater production at each grid cell and any rainfall on bare ground converted to an equivalent discharge (mm/m^2). Allowances have not been made for base flow, soil/groundwater recharge, nor refreezing of the liquid water constituent produced by lateral flow paths through the snowpack (Marsh and Woo, 1984; Kattleman and Dozier, 1999). From the onset of the modeling period through the early spring, catchment response as measured by runoff through the weir is substantially damped compared to simulated SWI. In this semi-arid region, it is quite likely that most meltwater reaching the ground during these early snowmelt events does not contribute to stream discharge (Flerchinger and Cooley, 2000). Once the ground presumably became saturated in early spring, the timing and magnitude of SWI closely matched the measured runoff at the weir (Figures 5b and 5c).

At the grove site, three discrepancies between modeled SWE (extracted from its corresponding grid cell) and measured SWE can be observed in Figure 5d. During early December when temperatures for the most part remained well below 0°C and storms were accompanied by moderate winds, the gain in mass atop the snow pillow was even less than that captured in the Alter-shielded rain gauge. Snow course measurements seemed to agree with the snow pillow data, inferring that perhaps an error in the precipitation data was the cause. In late February and early-mid March modeled snow water gain again exceeded the snow pillow measured accumulation. Two precipitation events during this period were accompanied by air temperatures that hovered around 0°C. ISNOBAL-modeled SWE accumulations in these storm periods were dependent upon the discrimination of precipitation into snow and rain components and proved to be highly sensitive to air temperature and relative humidity inputs. During this same timeframe, the relative humidity data captured at the ridge site was found to be questionable, requiring the substitution of

transformed data from a correlated RCEW site, conceivably causing the observed errors. Additionally, the modeled rate of melt during the final phase of melt-out appears a bit high. Given the previous successful applications of the point version of ISNOBAL to snow accumulation and melt at the grove site (Marks and Winstral, 2001), it was assumed that the observed errors during the 1986 water year were due primarily to problems with the forcing data rather than a model fault.

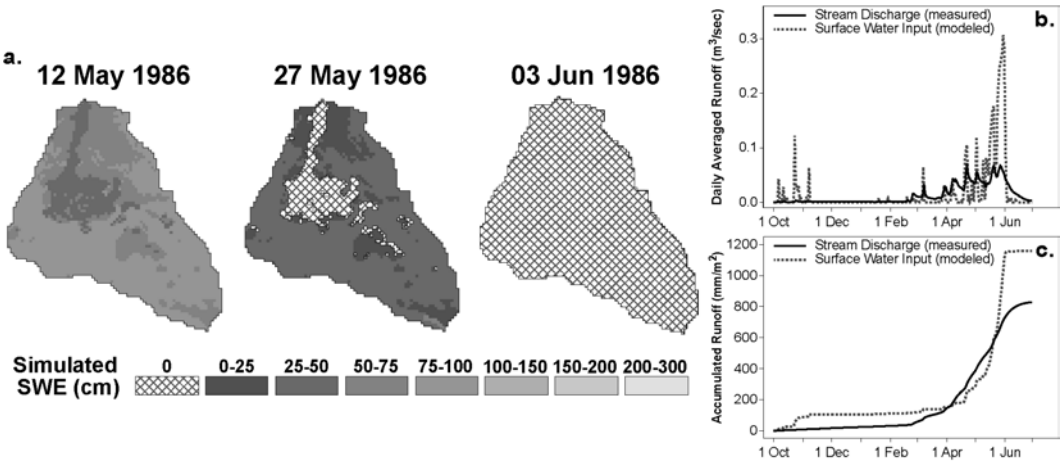

Figure 6. Simulated SWE forced with spatially constant precipitation and wind fields for the 1986 water year produced a relatively homogeneous snow cover (a) with a single peak to the hydrograph (b) while underestimating meltout prior to the simulated peak (c). Note that the scale of the y-axis in (b) has been increased by a factor of two relative to Figure 5b.

To point out the importance of accounting for intrabasin disparities in snow accumulation and turbulent energy fluxes in this headwater catchment, the 1986 water year was also modeled using meteorological inputs taken exclusively from the grove site. The grove site has characteristics similar to most snow telemetry (SNOTEL) sites in the western U.S., which are often the sole source of meteorological data from these mountainous regions. The product of this modeling exercise was a fairly homogeneous snow distribution (Figure 6a) with slight differences attributable to terrain and canopy effects on radiation fluxes. As expected, an all-at-once meltout of the snowpack was produced (c.f. Luce *et al.*, (1998)) with simulated snowmelt contributions to runoff concentrated in two events in late May (Figure 6b). The latter and largest of these two modeled events occurred 24May – 1June with most of the catchment contributing to runoff resulting in a greater than four-fold increase in simulated SWI compared to the model with distributed precipitation and wind fields applied previously (356 mm/m^2 vs. 77 mm/m^2). Aside from the over-prediction of peak runoff and the lack of late season snowmelt contributions from the drift areas produced by the spatially constant inputs, there was also a tendency to under-predict potentially devastating winter and early spring runoff events such as those produced by rain-on-snow events. In these events prior to the typical snowmelt season, oftentimes the greatest contributors to runoff are exposed areas with high turbulent energy exchanges whereas protected low energy areas have generally deeper and colder snowpacks that produce less snowmelt and have a greater capacity to absorb rainfall (Marks *et al.*, 1998; 2001; Marks et al., this issue). This latter phenomenon can be seen in the treatment of the mixed rain and snow event of 23February by the two models (Figures 5b and 6b) and over time in the crossover of the accumulated SWI and accumulated runoff plots beginning on 3April (Figure 6c). The model with the distributed precipitation and wind fields correctly predicted substantial SWI for the 23February runoff event that were derived primarily from the wind exposed regions (see Marks *et al.*, this issue), whereas the model forced with only the grove site data generated an insufficient amount of water.

4.3 1987 Water Year

The 1987 water year was the driest of the three simulation years with October – June precipitation at 66% of average and October – June stream discharge at 39% of average. The grove site was snow-free over a month earlier than it was in 1986. The spatial simulations (Figure 7a) again are in good agreement with the aerial photos. There appeared to be a slight southern bias to the geo-registration of the southeast section of the photos manifest in the location of the east and southeast drifts relative to their positions in photos from the other model years. Based on all available data from other years, the perceived early meltout of the southeast drift indicated by the 2May image is puzzling. We believe this to be an error due perhaps to the geo-registration or the classification process. Brightness levels in the original photographs may have been influenced during this dry winter by an increased accumulation of dirt atop the snow cover or the early emergence of the aspens that typically lie buried beneath this drift. In the 15April images it appeared that snow cover was being slightly under predicted along the southern boundary of the research area. This underestimation, also apparent in the 12May86 images, may be due to lateral flow divergence occurring leeward of the saddle between the two peaks defining the southern boundary of the watershed. The applied terrain parameters currently do not account for flow modifications of this type.

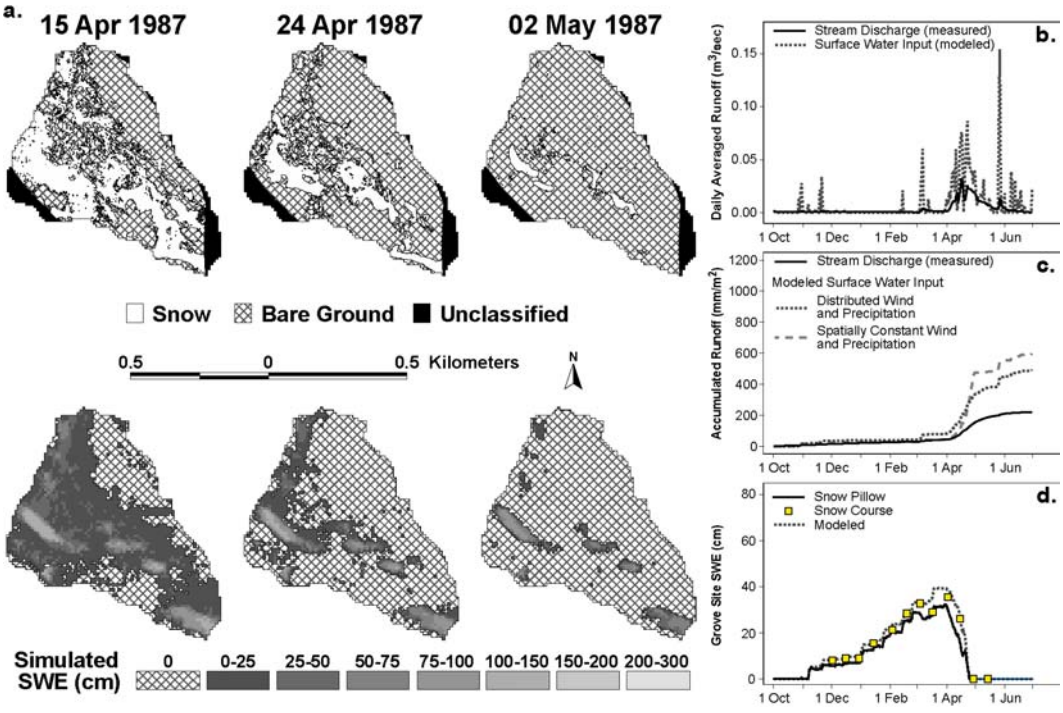

Figure 7. Comparisons of model results and validation data for the 1987 water year. (a) – (d) are as explained in Figure 5. In this dry year, basin response was consistently damped relative to simulated surface water inputs. The spatial simulations (a) and point simulations (d) are in good agreement while predicted inputs are correlated well with runoff (b and c).

During this dry winter, when soil water storage was conceivably never fully recharged, catchment response relative to simulated water inputs was constantly damped. Though the volumetric difference between modeled SWI and measured discharges during meltout were greater than those observed in 1986, the timing and relative magnitudes of modeled inputs correlated well with the basin hydrograph (Figures 7b and 7c). Also depicted in Figure 7c is accumulated runoff modeled with spatially constant wind and precipitation fields similar to the modeling depicted in Figure 6. Once again, a single large pulse of runoff is simulated using the spatially homogeneous snow accumulation and wind forcing data.

Modeled SWE at the grove site showed good agreement with the snow course data, with both measures exceeding that measured at the snow pillow (Figure 7d). Interestingly, the graphs of simulated and snow pillow SWE appeared similar to the 1986 plots (Figure 5d), however, in 1987 the snow course data differed from the pillow data and corroborated the modeled results.

4.4 1989 Water Year

The 1989 water year was slightly wetter than average with October – June precipitation 108% of average and stream discharge 123% of average. As in the previous modeling results, the simulated patterns of snow distribution showed good agreement with the classified photographs though snow cover seemed to be slightly underestimated in the modeled 12April and 3June images (Figure 8a). Similar to 1986 when precipitation was also above average, the timing and magnitude of the modeled SWI directly corresponded with the peaks of the basin hydrograph during the primary meltout period (Figures 8b and 8c). Simulated water inputs from the model forced with spatially constant wind and accumulation fields were once again concentrated in one surge and, as in 1986, were less than measured discharge immediately prior to the prime meltout period (Figure 8c). The simulated development and ablation of the snow cover at the grove site closely followed the snow course data, which as in 1987, was slightly greater than that measured by the snow pillow.

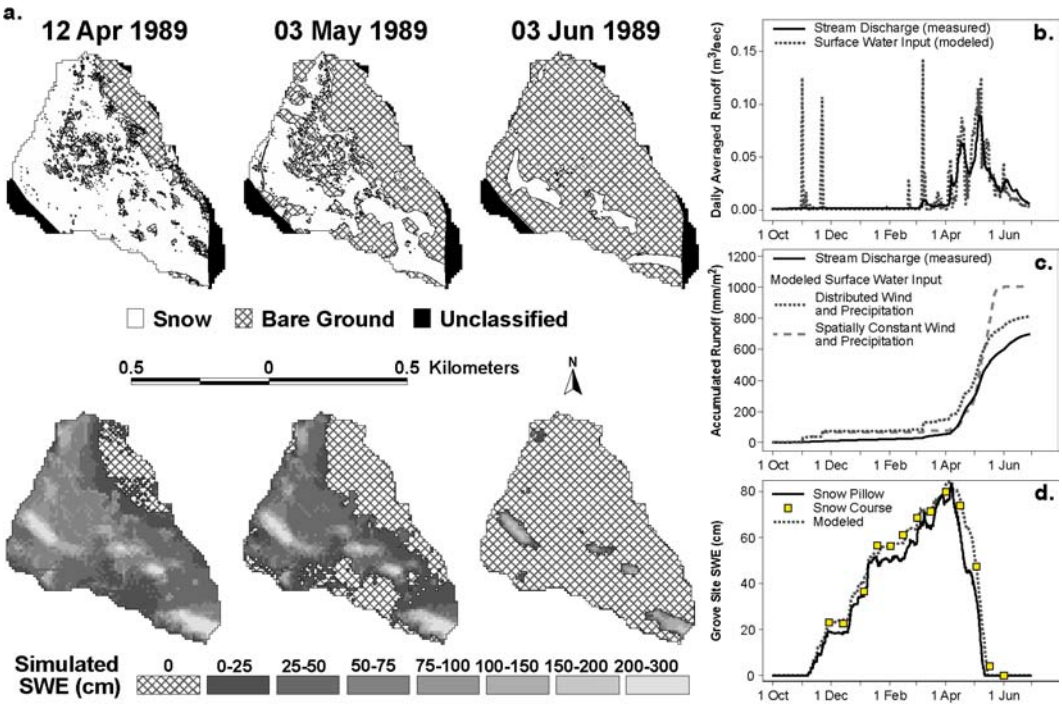

Figure 8. Comparisons of model results and validation data for the 1989 water year. (a) – (d) are as explained in Figure 5. Though the extent of the drifts seemed to be slightly underestimated in the 03 Jun images (a), the timing and magnitude of modeled surface water inputs (b and c) and predicted SWE at the grove site (d) showed excellent agreement with measured data.

5. CONCLUSIONS

A computationally efficient means of characterizing the effects of wind on snow accumulation and melt in mountainous terrain using terrain analysis was successfully developed and tested in a small headwater catchment where redistribution of snow is generally confined to storm periods. The presented terrain parameters quantified aspects of the upwind terrain related to wind exposure and snow accumulation and were combined with vegetation data to derive distributed snow and

wind fields to drive ISNOBAL, a distributed snow accumulation and melt model, at an hourly time-step. In all three test years, the presented methods simulated snow distributions that included drift and scour zones that were strongly correlated with observations.

As has been observed in other small mountain basins, the need to account for wind-induced heterogeneities in snow distribution and turbulent energy fluxes to accurately model basin hydrology was shown. In the two model years that were wetter than average, simulated surface water inputs averaged over the catchment directly correlated with measured discharge leaving the catchment once soils became saturated during spring meltout. In the dry model year, as during winter melt events in all three model years, though the timing and relative magnitudes of modeled surface water inputs showed good agreement with discharge, catchment response was damped relative to the modeled inputs. In this semi-arid environment where soil moisture levels are routinely well below field capacity entering the snow accumulation season, these latter results were not unexpected. Whereas ISNOBAL forced with distributed accumulation rates and wind speeds simulated a heterogeneous snow cover and water inputs consistent with observations, ISNOBAL forced with spatially constant accumulation rates and wind speeds simulated a relatively homogeneous snow cover, underestimated melt contributions prior to the main spring meltout period, and consistently predicted an all-at-once meltout inconsistent with observations.

In light of the simplified means employed to represent the extremely complex processes of windflow over alpine terrain and snow redistribution, the basic linear methods applied to distribute the point data as a function of the terrain parameterizations and vegetation data, and potential errors associated with the precision of the data-gathering instrumentation, the results of this research are very encouraging. The aerial photographs — cost effective, easily obtained, and in this case readily available — validated the spatial simulations only to the extent of information they provided; two-dimensional snapshots of snow extent depicting snow cover ablation during spring meltout. Further work has already been initiated (e.g. intensive basin snow surveys) to establish a robust spatial dataset to be used in future testing. These data will provide detailed spatial information on snow distribution throughout the season and should help to refine the straightforward interpolation techniques applied here. Our work has indicated that the terrain parameters, modeled herein from a 10 m grid scale DEM, are appropriate for modeling purposes up to at least the 30 m grid scale. Additional work will be necessary to address further upscaling.

REFERENCES

Anderson EA. 1976. A point energy and mass balance model of a snow cover. *National Weather Service Technical Report 19*. National Oceanic and Atmospheric Administration: Washington, DC; 150.

Balk B. and Elder K. 2000. Combining binary decision tree and geostatistical methods to estimate snow distribution in a mountain watershed. *Water Resources Research* 36(1): 13–26.

Barry RG. 1992. *Mountain Weather and Climate*. Routledge: London 2nd ed.; 402.

Barron JS, Band LE, Running SW, and Cline D. 1993. The effects of snow distribution on the hydrologic simulation of a high elevation Rocky Mountain watershed using Regional HydroEcological Simulation System, RHESSys. *Eos Transactions AGU* 74(43): 237.

Berg N. 1977. Prediction of natural snowdrift accumulation on alpine ridge sites. Ph. D. dissertation: University of Colorado, Boulder; 310.

Blöschl G, Kirnbauer R, and Gutknecht D. 1991. A spatially distributed snowmelt model for application in alpine terrain, In *Snow, Hydrology and Forests in High Alpine Areas*, IAHS-AIHS and IUGG XX General Assembly, Vienna, Austria, August 1991. Bergmann H, Lang H, Frey W, Issler D and Salm B (eds). IAHS Publication No. 105, IAHS: Wallingford; 51–60.

Blöschl G, and Kirnbauer R. 1992. An analysis of snow cover patterns in a small alpine catchment. *Hydrological Processes* 6: 99–109.

Byers HR. 1974. *General Meteorology*. McGraw-Hill: New York; 461.

Cline DW. 1992. Modeling the redistribution of snow in alpine areas using geographic information processing techniques. *Proceeding of Eastern Snow Conference*: 13–24.

Davis RE, Jordan R, Daly SF, and Koenig GG. 2001. Validation of snow models. In *Model Validation: Perspectives in Hydrological Science*, Anderson MG and Bates PD (eds). John Wiley and Sons Ltd.: 261–292.

Doesken NJ and Judson A. 1996. *The Snow Booklet: A Guide to the Science, Climatology, and Measurement of Snow in the United States*. Colorado State University Department of Atmospheric Science: Fort Collins, CO; 84.

Dozier J. 1980. A clear-sky spectral solar radiation model for snow-covered mountainous terrain, *Water Resources Research* 16(4): 709–718.

Dozier J and Frew J. 1981. Atmospheric corrections to satellite radiometric data over rugged terrain. *Remote Sensing of the Environment* 11: 191–205.

Dozier J, Bruno J, and Downey P. 1981. A faster solution to the horizon problem. *Computers and Geosciences* 7: 145–151.

Dubayah R. 1994. Modeling a solar radiation topoclimatology for the Rio Grande River Basin. *Journal of Vegetation Science* 5: 627–640.

Elder K, Dozier J, and Michaelsen J. 1991. Snow accumulation and distribution in an alpine watershed. *Water Resources Research* 27(7): 1541–1552.

Flerchinger GN and Cooley KR. 2000. A ten-year water balance of a mountainous semi-arid watershed. *Journal of Hydrology* 237: 86–99.

Hanson CL. 2001. Long-term precipitation database: Reynolds Creek Experimental Watershed, Idaho, United States. *Water Resources Research* 37(11): 2831–2834.

Hanson CL, Johnson GL, and Rango A. 1999. Comparison of precipitation catch between nine measuring systems. *Journal of Hydrologic Engineering*, 4(1): 70–75.

Hartman MD, Baron JS, Lammers RB, Cline DW, Band LE, Liston GE, and Tague C. 1999. Simulations of snow distribution and hydrology in a mountain basin. *Water Resources Research*. 35(5): 1587–1603.

Kattleman RC and Dozier J. 1999. Observations of snowpack ripening in the Sierra Nevada. *Journal of Glaciology* 45(151): 409–416.

Kind RJ. 1981. Snow drifting. Chapter 8 In *Handbook of Snow*, Gray D and Male D (eds). Pergamon: New York; 338–359.

Lapen DR and Martz LW. 1993. The measurement of two simple topographic indices of wind sheltering-exposure from raster digital elevation models. *Computers and Geosciences* 19(6): 769–779.

Link T and Marks D. 1999. Distributed simulation of snow cover mass- and energy-balance in the boreal forest. *Hydrological Processes* 13: 2439–2452.

Liston GE and Sturm M. 1998. A snow-transport model for complex terrain. *Journal of Glaciology* 44(148): 498–516.

Luce CH, Tarboton DG, and Cooley KR. 1998. The influence of the spatial distribution of snow on basin-averaged snowmelt. *Hydrological Processes* 12: 1671–1683.

Marks D. 1988. Climate, energy exchange, and snowmelt in Emerald Lake Watershed, Sierra Nevada. PhD Thesis: University of California at Santa Barbara; 158.

Marks D. 2001. Introduction to special section: Reynolds Creek Experimental Watershed. *Water Resources Research* 37(11): 2817.

Marks D and Dozier J. 1979. A clear-sky longwave radiation model for remote alpine areas. *Meteorologie, Geophysik und Bioklimatologie, Series B* 27(23): 159–187.

Marks D and Dozier J. 1992. Climate and energy exchange at the snow surface in the alpine region of the Sierra Nevada: 1. Meteorological measurements and monitoring. *Water Resources Research* 28: 3043–3054.

Marks D and Winstral A. 2001. Comparison of snow deposition, the snow cover energy balance, and snowmelt at two sites in a semiarid mountain basin. *Journal of Hydrometeorology* 2(3): 213–227.

Marks D, Kimball J, Tingey D, and Link T. 1998. The sensitivity of snowmelt processes to climate conditions and forest cover during rain-on-snow; a case study of the 1996 Pacific Northwest flood. *Hydrological Processes* 12, 1569–1587.

Marks D, Domingo J, Susong D, Link T, and Garen D. 1999a. A spatially distributed energy balance snowmelt model for application in mountain basins. *Hydrological Processes* 13: 1935–1959.

Marks D, Domingo J, and Frew J. 1999b. Software tools for hydro-climatic modeling and analysis: Image Processing Workbench, ARS-USGS version 2, *ARS Technical Bulletin 99-1*, Northwest Watershed Research Center, USDA Agricultural Research Service, Boise, ID. [Available online at http://www.nwrc.ars.usda.gov/ipw].

Marks D, Link T, Winstral A, and Garen D. 2001. Simulating snowmelt processes during rain-on-snow over a semi-arid mountain basin. *Annals of Glaciology* 32, 195–202.

Marsh P and Woo MK. 1984. Wetting front advance and freezing of meltwater within a snow cover 1. Observations in the Canadian Arctic. *Water Resources Research* 10(12): 1853–1864.

Marshall SE and Warren SG. 1987. Parameterizatoin of snow albedo for climate models. In *Large Scale Effects of Seasonal Snow Cover*. Goodison BE, Barry RG, and Dozier J (eds). IAHS-AIHS Publication No. 166, IAHS. Wallingford; 44–50.

Pomeroy JW, Gray DM, and Landine PG. 1993. The Prairie Blowing Snow Model: characteristics, validation, operation. *Journal of Hydrology* 144: 165–192.

Prasad R, Tarboton DG, Liston GE, Luce CH, and Seyfried MS. 2001. Testing a blowing snow model against distributed snow measurements at Upper Sheep Creek , Idaho, United States of America. *Water Resources Research* 37(5): 1341–1350.

Purves RS, Barton JS, Mackaness WA, and Sugden DE. 1998. The development of a rule-based spatial model of wind transport and deposition of snow. *Annals of Glaciology* 26: 197–202.

Robins JS, Kelly LL, and Hamon WR. 1965. Reynolds Creek in southwest Idaho: An outdoor hydrologic laboratory. *Water Resources Research* 1: 407–413.

Ryan BC. 1977. A mathematical model for diagnosis and prediction of surface winds in mountainous terrain. *Journal of Applied Meteorology* 16(6): 571–584.

Seyfried MS and Wilcox BP. 1995. Scale and the nature of spatial variability: Field examples having implications for hydrologic modeling. *Water Resources Research* 31(1): 173–184.

Slaughter CW, Marks D, Flerchinger GF, Van Vactor SS, and Burgess M. 2001. Thirty-five years of research data collection at the Reynolds Creek Experimental Watershed, Idaho, United States. *Water Resources Research* 37(11): 2819–2823.

Susong D, Marks D, and Garen D. 1999. Methods for developing time-series climate surfaces to drive topographically distributed energy- and water-balance models. *Hydrological Processes* 13: 2003–2021.

Tabler RD. 1994. Design guidelines for the control of blowing and drifting snow. *Report SHRP-H-381*. Strategic Highway Reseearch Program, National Research Council: Washington, D.C.; 364.

Tarboton DG, Al-adhami MJ, and Bowles DS. 1991. Preliminary comparisons of snowmelt models for erosion prediction. *Proceedings of Western Snow Conference*, 59: 79–90.

Tarboton DG and Luce CH. 1996. *Utah Energy Balance Snow Accumulation and Melt Model (UEB), Computer Model Technical Description and Users Guide*. Utah Water Research Laboratory: Logan, Utah; 41.

Tarboton DG, Blöschl G, Cooley K, Kirnbauer R, and Luce C. 2000. Spatial snow cover processes at Kühtai and Reynolds Creek. Chapter 7 In *Spatial Patterns in Catchment Hydrology: Observations and Modelling*. Grayson R and Blöschl G (eds). Cambridge University Press: UK; 158–186.

Warren SG and Wiscombe WJ. 1980. A model for the spectral albedo of snow. II: Snow containing atmospheric aerosols. *Journal of Atmospheric Science* 37: 2734–2745.

Winstral A. 1999. Implementation of digital terrain analysis to capture the effects of wind redistribution in spatial snow modeling. M.S. thesis: Colorado State University; 277.

Winstral A, Elder K, and Davis, RE. Spatial snow modeling of wind-redistributed snow using terrain-based parameters. *Journal of Hydrometeorolgy*, in press.

Wiscombe WJ and Warren SG. 1980. A model for the spectral albedo of snow. I: Pure snow. *Journal of Atmospheric Science* 37: 2712–2733.

Woolford RA, Bales RC, and Sorooshian S. 1996. Development of a hydrochemical model for seasonally snow-covered alpine watersheds: Application to Emerald Lake watershed, Sierra Nevada, California. *Water Resources Research* 32(4): 1061–1074.

Wörlen C, Schulz K. Huwe B, and Eiden R. 1999. Spatial extrapolation of agrometeorological variables. *Agricultural and Forest Meteorolgy* 94: 233–242.